



One-pot synthesis of bicrystalline titanium dioxide spheres with a core–shell structure as anode materials for lithium and sodium ion batteries



Zichao Yan, Li Liu^{*}, Jinli Tan, Qian Zhou, Zhifeng Huang, Dongdong Xia, Hongbo Shu, Xiukang Yang, Xianyou Wang^{*}

Key Laboratory of Environmentally Friendly Chemistry and Applications of Ministry of Education, School of Chemistry, Xiangtan University, Hunan, Xiangtan 411105, China

HIGHLIGHTS

- Anatase@TiO₂(B) spheres were firstly synthesized.
- Anatase@TiO₂(B) spheres show excellent electrochemical performance for Li insertion/extraction.
- Anatase@TiO₂(B) spheres also show excellent electrochemical performance for Na insertion/extraction.
- The excellent performance is due to the unique bicrystalline hierarchical structure.

ARTICLE INFO

Article history:

Received 14 May 2014

Received in revised form

28 June 2014

Accepted 29 June 2014

Available online 7 July 2014

Keywords:

Lithium ion batteries

Sodium ion batteries

Titanium dioxide

Bicrystalline hierarchical spheres

One-pot method

ABSTRACT

Bicrystalline titanium dioxide spheres (anatase@TiO₂(B) spheres) with enhanced electrochemical activity in lithium and sodium ion batteries have been successfully synthesized via a facile one-pot solvothermal method. The anatase@TiO₂(B) spheres have a core–shell structure with TiO₂(B) nanosheets sheathing the anatase TiO₂ sphere core which consists of nanoparticles, as characterized by X-ray diffraction, scanning electron microscopy (SEM), and high-resolution transmission microscopy (HRTEM). The anatase@TiO₂(B) spheres show excellent lithium storage performance, which have high initial discharge capacity (114.8 mAh g^{−1}) with almost no capacity fading after 100 cycles and still maintain at 91.7 mAh g^{−1} after 375 cycles at a super-high current density of 5040 mA g^{−1} (30 C). What's more, they also show excellent rate capability in sodium ion batteries at various current densities ranging from 85 to 850 mA g^{−1}. The unique hierarchical structure of anatase@TiO₂(B) spheres with excellent cycle performance and rate capability make a compelling case for their development as anode materials for both lithium and sodium ion batteries.

© 2014 Elsevier B.V. All rights reserved.

1. Introduction

Currently, environmental disruption and economic recession of burning non-renewable and unsustainable fossil fuels have gained a great deal of awareness of renewable energy storages [1,2]. Lithium ion batteries (LIBs) with superior electrochemical properties (e.g., large energy density, high rate capability, and long cycling life) have been considered of great valuable for commercial applications and theoretical studies [3]. However, its success is still limited due to their high cost on dollars per kilowatt hour basis [1].

Recently, sodium ion batteries (NIBs) with higher availability and potential for lower cost of raw materials have drawn scientists' attention [4]. As we all know, there are too many restrictions for these battery technologies, such as electrolytes, separators, and electrode materials. Among all of those restrictions, anode material is a crucial factor for both LIBs and NIBs in electrochemical property and safety [5,6]. Lithium and sodium insertion into carbon anode materials were extensively studied by a lot of scientists [7–9]. For LIBs, graphite is a widely used anode material in commercial lithium ion batteries, but it still has limitations and weaknesses, such as electrical disconnection, structural deformation and initial loss of capacity. Ti-based anode material with its inherent chemical stability, minimal toxicity, low cost, and high discharge potential has been considered as one of the most suitable candidates for LIBs

^{*} Corresponding authors. Tel.: +86 731 58292206; fax: +86 731 58292477.

E-mail addresses: liulili1203@126.com (L. Liu), wxianyou@yahoo.com (X. Wang).

anode materials [10,11]. Moreover, for NIBs, it is generally accepted that, unless high pressures are used, sodium insertion into graphitic carbons is minimal [12–14]. So, it is of great urgent for us to find a perfect anode material for both LIBs and NIBs, especially for future NIBs.

As a newly used anode material, TiO_2 with various crystalline polymorphs has been extensively studied in LIBs, and recent reports show the properties as Na hosts [15–17]. Although TiO_2 has many advantages as LIBs and NIBs anode material, the low ion diffusivity and poor conductivity badly affect the electrochemical property and restrict the widespread application of TiO_2 . What's more, crystalline phase, morphology, and size of particles also have important influence on its electrochemical properties.

Among various polymorphs of TiO_2 (rutile, anatase, brookite etc.), anatase TiO_2 with excellent electrochemical stability has attracted considerable interest due to its 3D networks. This structure leads to empty zigzag channels in the anatase framework, which not only gives possible interstitial sites for Li or Na accommodation, but also increases the electrochemical stability of anatase TiO_2 . Compared with anatase TiO_2 , $\text{TiO}_2(\text{B})$ with a relatively open tunnel structure and large interlayer spacing can provide a better electrochemical activity, which is also considered as a suitable active material for lithium storage and sodium ion intercalation [18–22]. However, the single phase of anatase TiO_2 or $\text{TiO}_2(\text{B})$ with good cycle performance or rate capability in LIBs have been found relative poor electrochemical performance in NIBs [18,19,21,23]. Considering that the bicrystalline of anatase TiO_2 and $\text{TiO}_2(\text{B})$ might contain both structural and electrochemical advantages of anatase TiO_2 and $\text{TiO}_2(\text{B})$. So, it would be of great interest to construct bicrystalline materials of anatase TiO_2 and $\text{TiO}_2(\text{B})$ with excellent electrochemical performance in LIBs and NIBs.

As for morphology and size, various nanosized TiO_2 with special morphologies, such as nanoribbons [13], nanotubes [21], nanosheets [22] and hollow nanospheres [24], have been fabricated to improve the specific capacity and rate performance. Even though nano-materials offer numerous advantages, such as huge surface area and high rate capability, they also have to suffer from low tap density, poor stability and serious side reactions [21]. Therefore, fabricating hierarchical micron-sized TiO_2 and $\text{TiO}_2\text{--C}$ composites have been considered as effective way to overcome these disadvantages and improve the electrochemical performance of TiO_2 [25,26]. Recently, micro-nanosized hierarchical structures composed with nano-sized assemblies and mesoporous nanoparticles with high packing density have been widely concerned by researchers owing to the multilevel and porous structure that can provide both extraordinarily high activated surface and robust stability [27–30]. So, electrode materials with hierarchical structure composed by nanosized particles can take the advantages of nanometer size effects, high tap density and high stability arisen from the micro- or sub-micro-sized assemblies, which could improve electrochemical property of electrode material remarkably. From the above aspects, it is of great significance to fabricate TiO_2 bicrystalline hierarchical spheres composed by nano-sized assemblies with high tap density and electrochemical activity from the view of both practical application and scientific research.

The conventional fabrication procedures of spherical structure generally involved templates, which related to tedious synthesis and high cost [31,32]. In this work, we synthesized the anatase@ $\text{TiO}_2(\text{B})$ hierarchical spheres with $\text{TiO}_2(\text{B})$ nanosheets sheathing anatase spheres core via a facile and green one-pot solvothermal method. The hierarchical structure contains the electrochemical advantages of bicrystalline structure and nanometer size effects. Moreover, it also increases the tap density and stability of the material due to the nano-sized assemblies and spherical

morphology. Here, we show the excellent electrochemical property of the anatase@ $\text{TiO}_2(\text{B})$ spheres for both LIBs and NIBs.

2. Experimental

2.1. Synthesis of anatase@ $\text{TiO}_2(\text{B})$ spheres

As shown in Fig. 1, anatase@ $\text{TiO}_2(\text{B})$ spheres were achieved via a one-pot facile solvothermal route. A mixture of 15 ml alcohol and 5 ml water was added dropwise into another mixture of 20 ml acetone solution of PVP and 5 ml tetrabutoxytitanium until no more white precipitate of titanium hydroxide was produced. After the solution was gently stirred for 2 h at room temperature, 5 ml NaOH solution (1.25 M) were added dropwise into the white suspension. After the suspension was stirred vigorously for 3 h at room temperature, the reaction suspension was then transferred to a 100 ml Teflon-lined stainless steel autoclave and kept in an electric oven at 180 °C for 6 h. The white precipitate was rinsed with distilled water, 0.1 M HCl, and distilled water until pH 7 was reached. After drying at 80 °C for at least 1 day, the as-prepared sample was calcined in a tubular furnace at 450 °C for 4 h in air to remove residual organics, and anatase@ $\text{TiO}_2(\text{B})$ spheres were obtained. In order to investigate the effect of different amount of NaOH solution, 2.5 ml and 7.5 ml NaOH solution were used to observe the change of TiO_2 . For comparison, anatase TiO_2 spheres were also prepared in the same way except for the addition of NaOH solution.

2.2. Structure and morphology characterization

The structures of the as-synthesized samples were characterized by X-ray diffraction. X-ray powder diffraction data were obtained using a Rigaku D/MAX-2500 powder diffractometer with a graphite monochromatic and Cu K α radiation ($\lambda = 0.15418$ nm) operated at a scan rate of 5° min^{−1} in the 2 θ range of 10°–80°. Scanning electron microscope (SEM) images of the samples were collected using a JEOL JSM-6610 scanning electron microscope, which were used to observe the morphology of the samples. Besides, high-resolution transmission electron microscopy (HRTEM) and fast-Fourier transform (FFT) measurements were carried out using a JEOL JEM-2100F transmission electron microscope at an acceleration voltage of 200 kV.

2.3. Electrochemical characterization

The working electrodes for lithium and sodium cells were fabricated by mixing the as-synthesized samples, carbon black, and Polyvinylidene fluoride (PVDF) binder with a weight ratio of 70:20:10 in N-methyl pyrrolidinone, which were then pasted on copper foil followed by drying under vacuum at 110 °C for 10 h. For lithium cells, the testing cells were assembled with the working electrode thus fabricated, metallic lithium anode, Celgard 2300 film separator and 1 M LiPF_6 in 1:1 ethylene carbonate (EC)/dimethyl carbonate (DMC) electrolyte, whereas sodium cells were assembled with metallic sodium as the negative electrode, glass fiber separator (Whatman GF/D), and 1 M NaClO_4 in propylene carbonate (PC) electrolyte. The assembly of the testing cells was carried out in an argon-filled glove box, where water and oxygen concentration were kept less than 5 ppm. The charge–discharge cycle tests of LIBs (168 mA g^{−1} was assumed to be 1 C rate) and NIBs were run at different current densities between 1.0–3.0 V and 0.01–2.5 V, respectively. All the cells were allowed to age for overnight before testing.

Cyclic voltammetry (CV) tests and EIS experiments were performed on a Zahner Zennium electrochemical workstation. CV tests

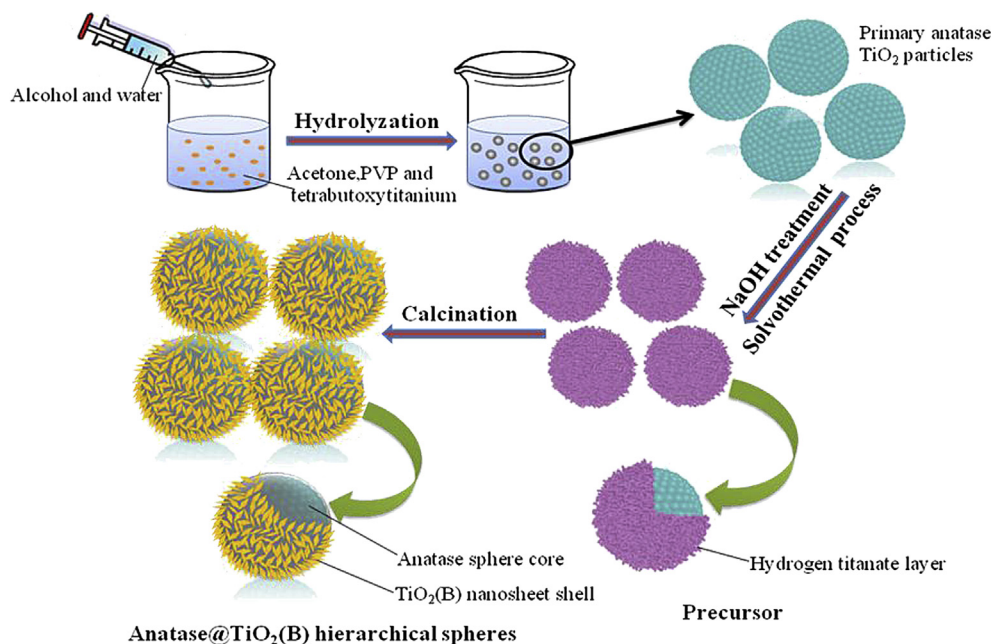


Fig. 1. Schematic illustration for the formation of anatase@TiO₂(B) spheres' microstructure.

were carried out at a scan rate of 0.1 mV s^{-1} on the potential interval 1.4–2.4 V (vs. Li⁺/Li) and 0.01–2.5 V (vs. Na⁺/Na). The ac perturbation signal was $\pm 5 \text{ mV}$ and the frequency range was from 10 mHz to 100 KHz. All the tests were performed at room temperature.

3. Results and discussion

3.1. Characterization of anatase@TiO₂(B) spheres

The X-ray diffraction (XRD) measurement was used to study phase composition and purity of the products. Fig. 2 shows the XRD pattern of the prepared anatase TiO₂ spheres without adding NaOH and anatase@TiO₂(B) spheres with adding 5 ml NaOH in the synthesis process. The anatase TiO₂ spheres display good crystal

structure, of which the diffraction peaks in the XRD pattern can be indexed well based on anatase phase corresponding to JCPDS No. 21-1272. However, some minor peaks are obviously observed from anatase@TiO₂(B) spheres, which can be identified as monoclinic TiO₂(B) phase (JCPDS No. 35-0088) and marked with asterisk. The weak peaks of TiO₂(B) in the final material can originate from the initial precursor treated by NaOH. This hydrothermal treatment of TiO₂ in NaOH medium to synthesize TiO₂(B) was pioneered by Kasuga et al. [33,34] in 1998. The treatment by NaOH that reacted with the surface of the initial precursor changed the structure of initial precursor, resulting in the partial transformation from anatase phase TiO₂ to TiO₂(B) during heat treatment, which is similar to that noted in previous reports [35,36]. Other XRD patterns of TiO₂ treated by different amount of NaOH (2.5 ml, 7.5 ml) are shown in Fig. S1 (see Supporting information). It is strange that the bicrystalline hierarchical sphere can be found only by adding 5 ml NaOH in the synthesis process. This phenomenon indicate that the amount of NaOH play an important role in forming bicrystalline hierarchical sphere, such as influence the PH or reaction degree, but the specific reason causing this phenomenon remains to be studied.

The morphology of anatase TiO₂ spheres and anatase@TiO₂(B) spheres is displayed in Fig. 3. As shown in Fig. 3a, the SEM image of anatase TiO₂ spheres reveals the distribution of inhomogeneous spheres with relative smooth surface and diameters ranging from 0.2 to 5.0 μm . After NaOH treatment, particles are getting smaller and quite uniform. The distribution of well-defined precursor of anatase@TiO₂(B) hierarchical spheres are shown in Fig. S2a. The surface of the particles is changed from smooth to rough and the hierarchical structure also initially formed. The anatase@TiO₂(B) spheres can be observed after annealing, and the constituent nanosheets on the surface of the spheres are clearly visible and show to adopt random orientations (see Fig. 3b). Compared with anatase TiO₂, the anatase@TiO₂(B) spheres composed with nano-sized assemblies show better regularity and smaller size with diameters ranging from 0.5 to 2.0 μm . Other SEM images of TiO₂ treated by different amount of NaOH (2.5 ml, 7.5 ml) can be found in Fig. S2b and c. These images indicate that the structure of hierarchical sphere with adding moderate volume of NaOH (5 ml) is much better than the others. This phenomenon also indicates that the

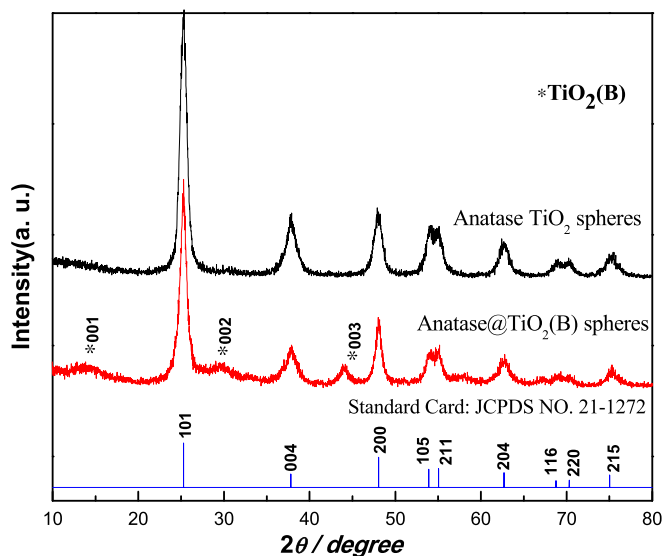


Fig. 2. XRD patterns of anatase TiO₂ spheres and anatase@TiO₂(B) spheres.

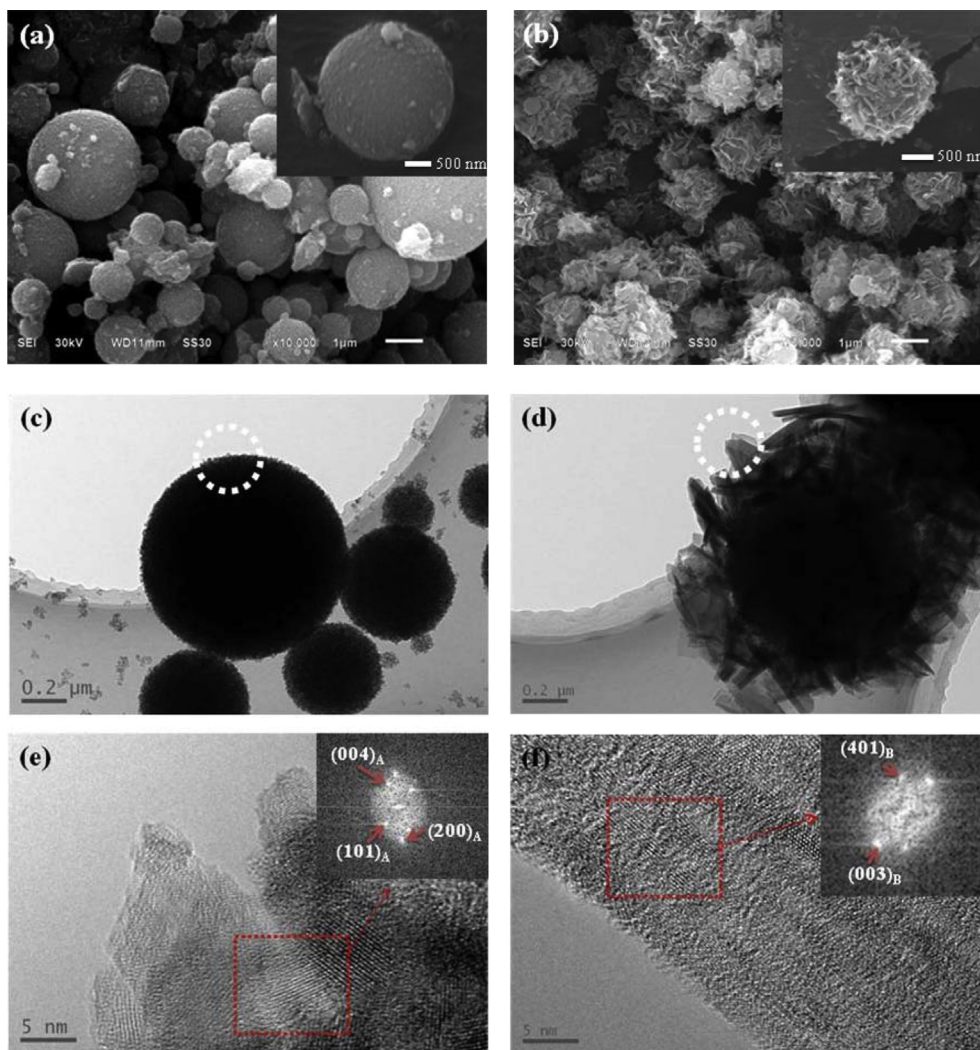


Fig. 3. SEM (a), TEM (c) and HRTEM (e) images of anatase TiO₂ spheres; SEM (b), TEM (d) and HRTEM (f) images of anatase@TiO₂(B) spheres. The insets show the corresponding FFT patterns. (Subscripts 'A' and 'B' represent the 'anatase' and 'TiO₂(B)', respectively.)

amount of NaOH is of crucial importance in the synthesis process of forming bicrystalline hierarchical sphere.

In order to further investigate morphology and structure of the final products, TEM, HRTEM, and fast-Fourier transform (FFT) images of anatase TiO₂ spheres and anatase@TiO₂(B) spheres are shown in Fig. 3c–f. In the TEM image, it can be found that anatase TiO₂ spheres are constituted by TiO₂ nanoparticles (see Fig. 3c). However, anatase@TiO₂(B) spheres are composed of spheres core and nanosheets shell, and the spherical nature of anatase@TiO₂(B) is still clear even though nanosheets are grown on the surface of the spheres (see Fig. 3d). If the reaction temperature is raised or time is extended, this core–shell structure can be observed more clearly but incomplete (see Fig. S2d–f). HRTEM (see Fig. 3e and f) analysis is employed to determine the crystal facets. Fig. 3e shows that anatase TiO₂ spheres display clear crystal lattices, its FFT image of the same region (inset) reveals that the diffraction spots have a lattice spacing related to the (101), (004) and (200) planes, corresponding to anatase TiO₂. In addition, the HRTEM image of anatase core which is separated from anatase@TiO₂(B) spheres is shown in Fig. S2g. Its FFT image shows the same diffraction spots with anatase TiO₂ spheres (see Fig. 3e), which indicates the phase of the core of anatase@TiO₂(B) spheres still retains anatase phase. Accordingly, the HRTEM image of nanosheets being part of

anatase@TiO₂(B) spheres is shown in Fig. 3f. It can be found that the nanosheet has a relative blurry crystal lattice, and the diffraction spots with lattice spacing related to the (401) and (003) planes of TiO₂(B) phase, namely, the FFT image demonstrate the existent of TiO₂(B) phase. This is well agreement with the XRD measurement of anatase@TiO₂(B) spheres where small amount of TiO₂(B) phase coexists with the anatase phase. Therefore, it can be concluded that the anatase@TiO₂(B) spheres are composed of anatase sphere core and TiO₂(B) nanosheet shell.

3.2. Electrochemical studies in lithium ion batteries

The comparison of electrochemical performance of anatase TiO₂ and anatase@TiO₂(B) as lithium insertion electrodes were studied to examine the effectiveness of bicrystalline hierarchical structure in improving the electrochemical performance of TiO₂ electrode. Fig. 4 shows the cycle performance and charge/discharge profiles (insets) of anatase TiO₂ spheres and anatase@TiO₂(B) spheres. As shown in Fig. 4a, the discharge capacity of anatase TiO₂ spheres drops from 198 to 112.9 mAh g^{−1} sharply after 100 cycles, with a large capacity loss of 45%. It is apparent that the anatase TiO₂ spheres shows a huge irreversible capacity loss on the first cycle and low capacity retention after 100 cycles. On the contrary,

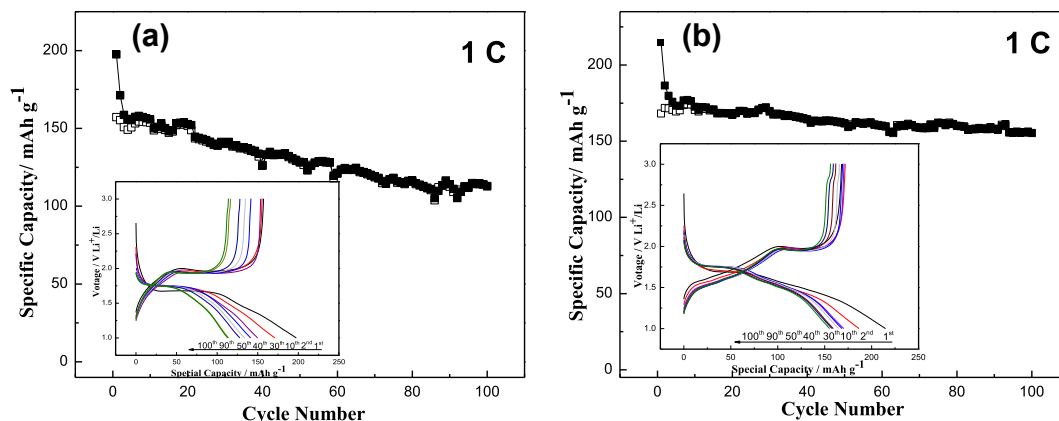


Fig. 4. Variation of charge (hollow) and discharge (solid) capacity vs. cycle number and charge/discharge profiles (the insets) for the (a) anatase TiO_2 spheres and (b) anatase@ $\text{TiO}_2(\text{B})$ hierarchical spheres at a current density of 168 mA g^{-1} (1 C) in the range of 1.0 V–3.0 V in Li half-cells.

anatase@ $\text{TiO}_2(\text{B})$ spheres can deliver discharge capacity of 214.7 mAh g^{-1} (1 C) at the first discharge process, and the capacity of 155.2 mAh g^{-1} is finally remained after 100 cycles (see Fig. 4b). The capacity of anatase@ $\text{TiO}_2(\text{B})$ spheres decreases in the first several cycles and it turns to be stable in the following cycles, which indicates far better cycling performance. Notably, the charge/discharge voltage profile of anatase@ $\text{TiO}_2(\text{B})$ electrode (see inset in Fig. 4b) demonstrate a low irreversible capacity loss of 21% at the first cycle, which is relatively lower than other anatase TiO_2 electrodes with 30–40% [37,38]. With the increase of the cycle number, the Coulombic efficiency of anatase@ $\text{TiO}_2(\text{B})$ spheres increases rapidly. Take the second and fourth cycle as example, the value of Coulombic efficiency rises to 92% in the second cycle and this value turns to 97% in the fourth cycle. This phenomenon is due to that the trapping of Li^+ inside the TiO_2 framework decreases rapidly upon cycling [39]. In addition, the anatase@ $\text{TiO}_2(\text{B})$ spheres show similar behaviors with the anatase TiO_2 spheres (see inset in Fig. 4a), where two voltage plateaus locate at 1.7 and 2.0 V during the discharge and charge processes, respectively. However, the charge/discharge voltage profiles of anatase@ $\text{TiO}_2(\text{B})$ spheres present another voltage plateaus in the voltage range of 1.5–1.7 V, which is maybe due to the characteristic plateaus of $\text{TiO}_2(\text{B})$ and will be further proved by the cyclic voltammetry (CV) tests.

To illustrate the outstanding rate performance of anatase@ $\text{TiO}_2(\text{B})$ hierarchical spheres, the cells are cycled at various rates ranging from 5 C to 30 C, as shown in Fig. 5. Anatase@ $\text{TiO}_2(\text{B})$ hierarchical spheres can deliver discharge capacity of 173.1 mAh g^{-1} (5 C), 136.6 mAh g^{-1} (10 C) and 114.8 mAh g^{-1} (30 C) at the first discharge capacity, and 154.6 mAh g^{-1} (5 C), 131.1 mAh g^{-1} (10 C) and 107.8 mAh g^{-1} (30 C) are finally remained after 100 cycles, which is far better than the electrochemical performance of anatase spheres treated by other amount of NaOH solution (see Fig. S3). Remarkably, the hierarchical spheres have excellent capacity retention over extended cycling even at high rates. The outstanding rate performance of anatase@ $\text{TiO}_2(\text{B})$ hierarchical spheres can be greatly attributed to the robust stability of the micro-nanosized structure of hierarchical spheres which consist of $\text{TiO}_2(\text{B})$ nanosheets and anatase nanoparticles. This special structure can decrease diffusion path and provide highly efficient solid-state diffusion of Li^+ ions [3]. Lithium cell made using anatase@ $\text{TiO}_2(\text{B})$ spheres is run at 30 C for 375 cycles to test the long term cyclability of materials at the high rates (see the inset in Fig. 5). The discharge capacity starts at 114.8 mAh g^{-1} and still maintains at 91.7 mAh g^{-1} after 375 cycles, with a capacity loss of only 20%. The super cycling performance and high specific capacity at ultra-fast discharging/

charging indicate the super structure stability of hierarchical spheres and pseudocapacitive behavior of $\text{TiO}_2(\text{B})$ nanosheets during lithium insertion-extraction [22]. These results greatly suggest that the excellent electrochemical performance of anatase@ $\text{TiO}_2(\text{B})$ spheres can be widely employed in the research and development for LIBs improvement.

Fig. 6 displays the representative CV curves of anatase TiO_2 and anatase@ $\text{TiO}_2(\text{B})$, respectively. As shown in Fig. 6a, The voltammogram of anatase TiO_2 shows a pair of well-defined reduction/oxidation peaks observed at 1.70 V (reduction peak) and 2.01 V (oxidation peak), which can be attributed to the discharge and charge processes of the Li^+ into/out of the anatase framework [40,41]. It is apparent that the voltammogram of anatase@ $\text{TiO}_2(\text{B})$ (see Fig. 6b) is dominated by a pair of peaks (A), which agrees with the peaks of anatase TiO_2 . Reduction and oxidation potentials of the remaining two pairs of peaks denoted as S1 and S2 are 1.48 V/1.54 V and 1.54 V/1.61 V vs Li^+/Li , respectively. The remaining two pairs (S1, S2) reflect the characteristic pseudo-capacitive behavior of lithium storage in $\text{TiO}_2(\text{B})$ [42,43]. The pseudo-capacitive behavior originates from the unique sites and energetic of lithium

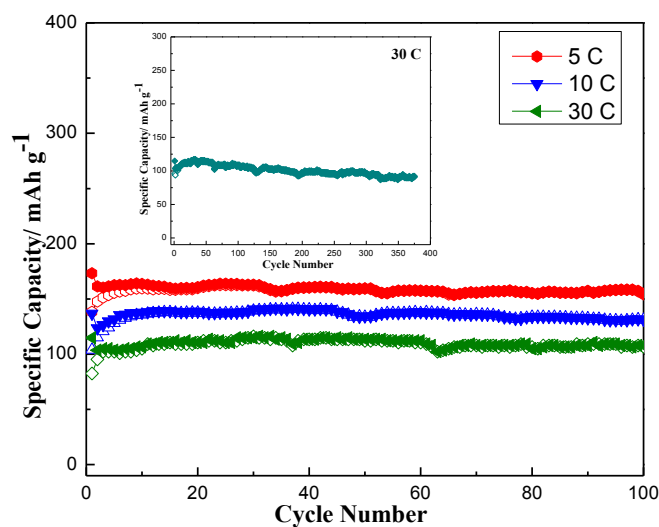


Fig. 5. Variation of charge (hollow) and discharge (solid) capacity vs. cycle number at 5 C, 10 C, 30 C and long term cycling performance (the inset) at 30 C for anatase@ $\text{TiO}_2(\text{B})$ spheres in the range of 1.0 V–3.0 V in Li half-cells.

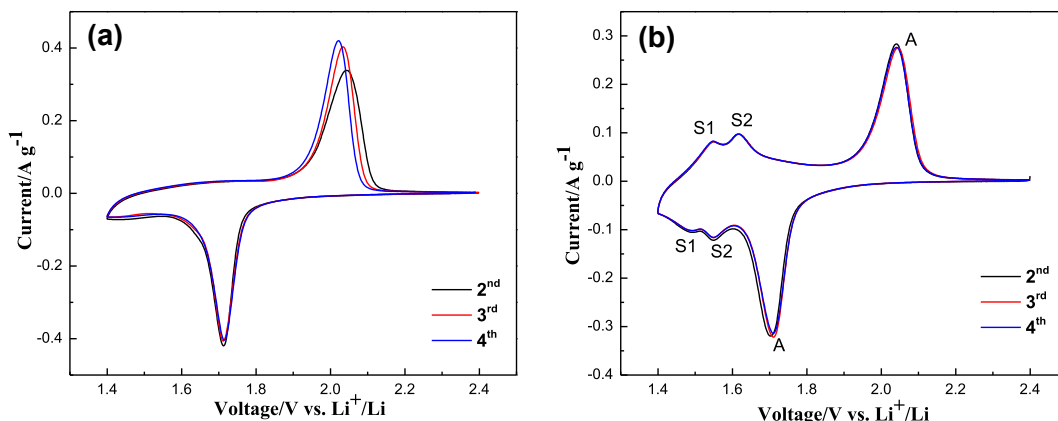


Fig. 6. Cyclic voltammogram of (a) anatase TiO_2 spheres and (b) anatase@ $\text{TiO}_2(\text{B})$ spheres at a scan rate of 0.1 mV s^{-1} between 1.4 and 2.4 V.

absorption and diffusion in the $\text{TiO}_2(\text{B})$ structure, which have been studied by theoretical studies [44,45]. The voltammogram of anatase@ $\text{TiO}_2(\text{B})$ spheres agrees well with XRD (see Fig. 2) and HRTEM (see Fig. 3f) about the presence of $\text{TiO}_2(\text{B})$ phase, and it also demonstrate that the voltage plateaus of charge/discharge voltage profiles (see the inset in Fig. 4b) located at the range of 1.5–1.7 V can be attributed to the processes of the Li^+ into and out of the $\text{TiO}_2(\text{B})$ phase. Therefore, the extra peaks (S-peaks) can be assigned to $\text{TiO}_2(\text{B})$, which are in good agreement with other reports [44,46]. Moreover, with the cycle number increasing, the peak current densities are almost changeless and the curves are nearly identical (see Fig. 6b), indicating the bicrystalline hierarchical sphere shows excellent cycle performance. This is in accordance with the long term cycling stability of anatase@ $\text{TiO}_2(\text{B})$ spheres.

The three-dimensional Nyquist plots of anatase TiO_2 and anatase@ $\text{TiO}_2(\text{B})$ after cycling for different cycles at around 2.0 V are shown in Fig. 7a and b. The EIS is recorded during 1st to 40th charge/discharge cycles at room temperature. The shapes of the Nyquist plots for each cycle are similar. The EIS pattern is mainly composed of one semicircle in the high frequency region and a sloping line in the low frequency region. Nyquist plots are fitted using the equivalent circuit model (see Fig. 7c), and the fitted impedance data are listed in Table 1. The fitting patterns show that fitting data are in well agreement with experimental data as shown in Fig. 7a and b. The equivalent circuit model includes R_s , a constant phase element (CPE) associated with the interfacial resistance, and the semi-circle is correlated with the lithium charge transfer resistance at the interface R_{ct} . R_s plays an important role in the model, it denotes the intrinsic resistance of the active material, the ionic resistance of the electrolyte and the contact resistance at the interface active material/current collector. It is explicit from Table 1 that the R_s and R_{ct} of anatase@ $\text{TiO}_2(\text{B})$ are smaller than those of anatase TiO_2 , implying that the anatase@ $\text{TiO}_2(\text{B})$ has higher conductivity and faster lithium ion diffusion than anatase TiO_2 sample. The linear portion is designated to Warburg impedance (Z_w), which is attributed to the diffusion of lithium ion into the bulk of the electrode materials. The lithium ion diffusion coefficient can be calculated according to the following equation [47–49]:

$$D = \frac{R^2 T^2}{2A^2 n^4 F^4 c^2 \sigma_w^2} \quad (1)$$

where R is the gas constant, T is the absolute temperature, A is the surface area of the cathode, n is the number of electrons per molecule during oxidation, F is the Faraday constant, C is the

concentration of lithium ion, and σ_w is the Warburg factor which is relative with Z' .

$$Z' = R_s + R_{ct} + \sigma_w \omega^{-1/2} \quad (2)$$

where ω is the angular frequency in the low frequency region. The relationship plot between Z_{re} and reciprocal square root of the angular frequency ($\omega^{-1/2}$) at low-frequency region is shown in Fig. 7d. The lithium ion diffusion coefficients (D_{Li}) of anatase@ $\text{TiO}_2(\text{B})$ after 10 cycles calculated by Eqs. (1) and (2) is $8.33 \times 10^{-13} \text{ cm}^2 \text{ s}^{-1}$ which is higher than that of anatase TiO_2 ($6.92 \times 10^{-13} \text{ cm}^2 \text{ s}^{-1}$). The R_{ct} of anatase TiO_2 sample is 60.0Ω after one cycle, and this value increases to 220Ω after 40 cycles. However, the R_{ct} of the anatase@ $\text{TiO}_2(\text{B})$ is 50.5Ω after one cycle, and this value only increases to 89.7Ω after 40 cycles. It is well-known that the lower increase of impedance during cycling means lower polarization, which indicates good cycling behavior. These results are consistent with the excellent electrochemical performance of anatase@ $\text{TiO}_2(\text{B})$ spheres.

3.3. Electrochemical studies in sodium ion batteries

Various electrochemical analysis of anatase@ $\text{TiO}_2(\text{B})$ spheres in NIBs are studied to demonstrate their viability and applicability as anode material for NIBs. The cycle performance of anatase@ $\text{TiO}_2(\text{B})$ spheres is shown in Fig. 8a. The discharge capacity starts at 375.4 mAh g^{-1} and it turns to be 234.2 mAh g^{-1} in the second cycle at a current density of 170 mA g^{-1} . There is a substantial capacity loss during the first several cycles. This may be associated with SEI formation and some form of irreversible trapping of Na by the TiO_2 lattice [18]. However, the capacity decreases in the first several cycles and discharge capacity of about 135 mAh g^{-1} remains almost entirely stable during cycling for 50 times at a current density of 170 mA g^{-1} . What's more, with the increasing of the cycle numbers, the charge capacity of anatase@ $\text{TiO}_2(\text{B})$ spheres is getting stable and the coulombic efficiency is nearly 100% after the first several cycles. The inset in Fig. 8a shows the charge/discharge voltage profiles of anatase@ $\text{TiO}_2(\text{B})$ spheres for the 1st, 2nd, 20th, 30th and 50th cycles at a current density of 170 mA g^{-1} in the voltage range of 0.01–2.5 V. The sample shows sloped reaction plateaus of 0.7 V and 0.9 V, which delegates representative discharge/charge profiles of TiO_2 electrode in NIBs [18,23]. It displays an initial discharge capacity of 375.4 mAh g^{-1} and a corresponding charge capacity of 167.4 mAh g^{-1} , showing a lower initial coulombic efficiency than that in LIBs. This can be connected with the irreversible capture of sodium during the first cycle on the surface and inside of the

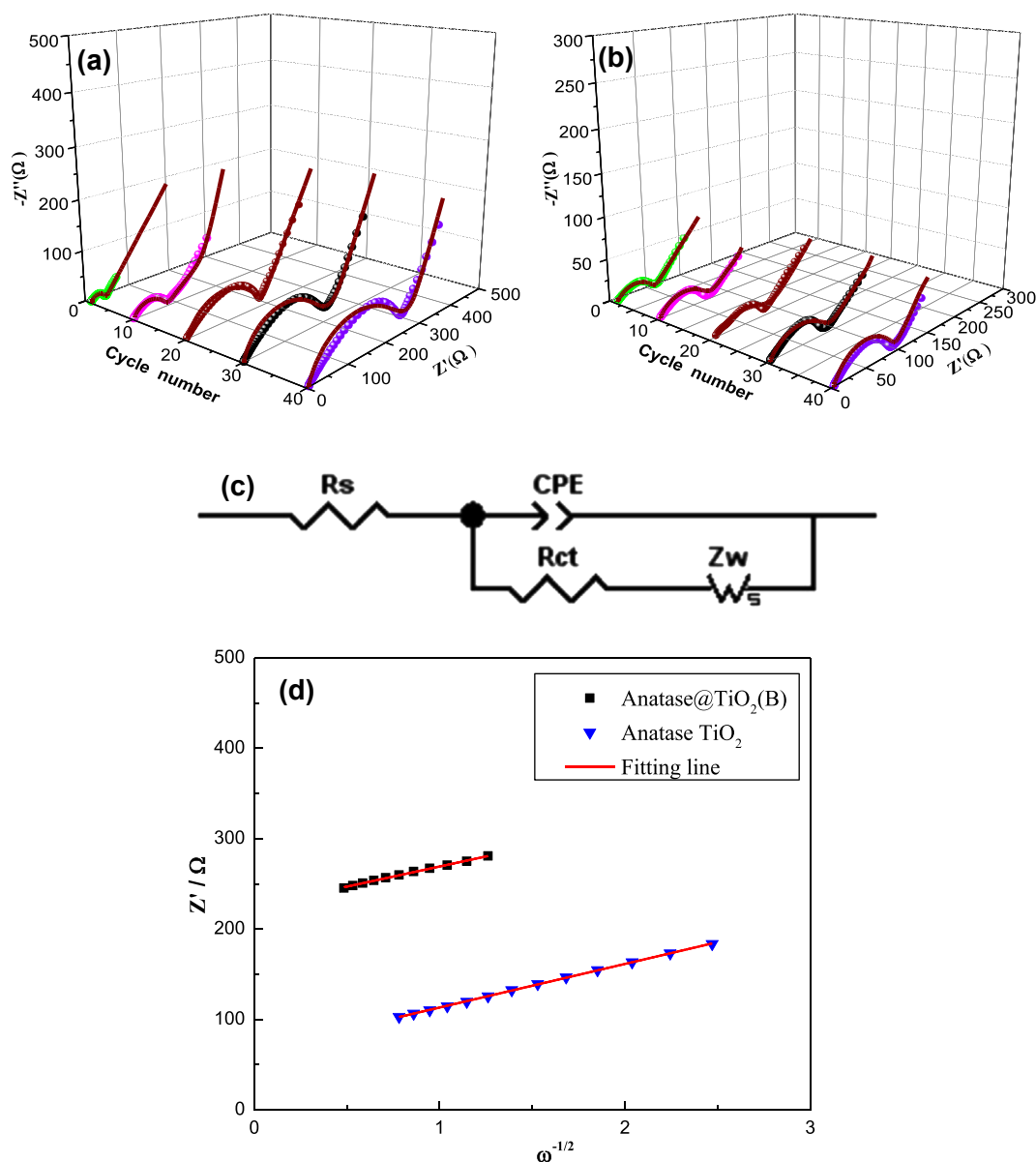


Fig. 7. Three-dimensional Nyquist plots measured for (a) anatase TiO_2 spheres and (b) anatase@ $\text{TiO}_2(\text{B})$ spheres after cycling for different cycles at 1 C in Li half-cells; (c) the equivalent circuit model; (d) the relationship plot between Z_{re} and $\omega^{-1/2}$ at low-frequency region.

anatase@ $\text{TiO}_2(\text{B})$ spheres interlayer. However, the efficiency increases dramatically after several cycles (over 94%), showing good capacity retention. The rate capability of anatase@ $\text{TiO}_2(\text{B})$ spheres for NIBs is further investigated at various current densities ranging from 85 to 850 mA g^{-1} as shown in Fig. 8b. At the current density of 85 mA g^{-1} , the material delivers a large discharge capacity of 173.2 mAh g^{-1} . When increasing the current densities to 170, 340 and 850 mA g^{-1} , discharge capacities of 142.6, 135.3 and 104.5 mAh g^{-1} are obtained respectively. After deep cycling at high

rates, a capacity of 168.6 mAh g^{-1} is fully restored upon reducing the current density to 85 mA g^{-1} , indicating good rate capability of anatase@ $\text{TiO}_2(\text{B})$ spheres as anode materials for the NIBs. The excellent electrochemical performance of anatase@ $\text{TiO}_2(\text{B})$ spheres in NIBs indicates that the anatase@ $\text{TiO}_2(\text{B})$ spheres are optimal candidates for NIBs.

To further explore the sodium ion insertion–extraction behavior of anatase@ $\text{TiO}_2(\text{B})$ hierarchical spheres for anode active material of NIBs, the CV curves of anatase@ $\text{TiO}_2(\text{B})$ hierarchical spheres are

Table 1

R_s and R_{ct} values of anatase TiO_2 spheres and anatase@ $\text{TiO}_2(\text{B})$ spheres after different cycles in Li half-cells.

Samples	R_s (Ω)					R_{ct} (Ω)				
	1st	10th	20th	30th	40th	1st	10th	20th	30th	40th
Anatase	2.81	3.74	5.93	6.30	6.43	60.0	72.8	175	180	220
Anatase@ $\text{TiO}_2(\text{B})$	3.76	4.01	4.40	4.36	4.52	50.5	67.5	82.2	84.2	89.7

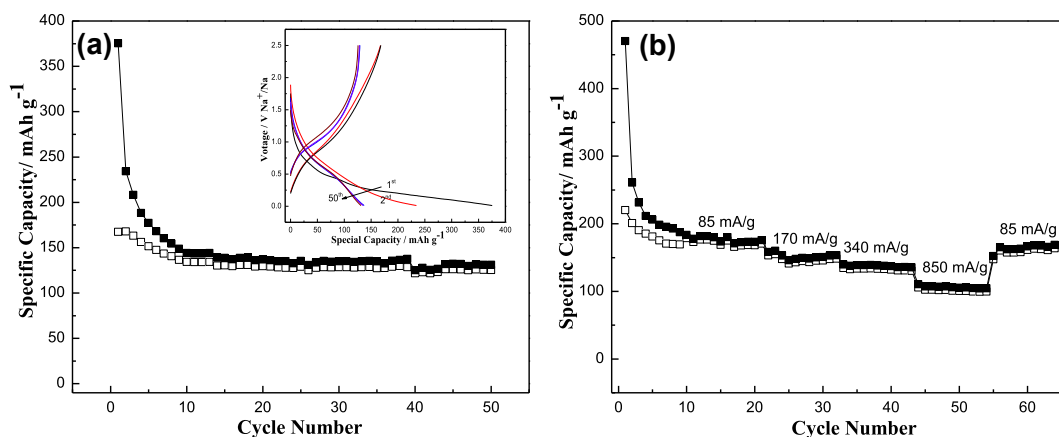


Fig. 8. (a) Variation of charge (hollow) and discharge (solid) capacity vs. cycle number and charge/discharge profiles (insets) at a current density of 170 mA g⁻¹ and (b) rate capability at 85–850 mA g⁻¹ for anatase@TiO₂(B) spheres in the range of 0.01 V–2.5 V in Na half-cells.

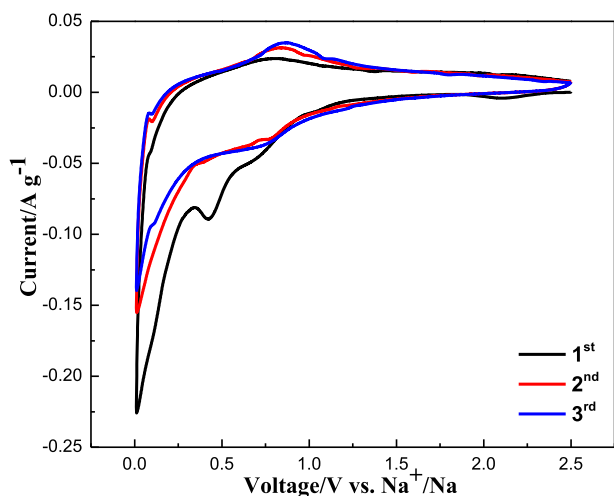


Fig. 9. Cyclic voltammogram of anatase@TiO₂(B) spheres electrode at a scan rate of 0.1 mV s⁻¹ between 0.01 and 2.5 V.

shown in Fig. 9. The reduction peak at 0.42 V appears in the first cycle and disappears after the second cycle which also can be assigned to irreversible formation of the SEI films and trapping of Na by the TiO₂ lattice just as in LIBs. By the following cycles, a pair of redox peaks observed at 0.65 V (reduction peak) and 0.86 V (oxidation peak) becomes remarkable, which is well agreement with the charge/discharge voltage profiles (see the inset in Fig. 8a) and other reports [18].

The three-dimensional Nyquist plot is carried out to gain further insight into electrode microstructural changes during cycling in NIBs (see Fig. 10a). The EIS is recorded during 1st to 40th charge/discharge cycles. Nyquist plot is fitted using the equivalent circuit model which is the same as LIBs (see Fig. 10b), and the fitted impedance data are listed in Table 2. The R_{ct} (transfer resistance) of anatase@TiO₂(B) is 75 Ω after one cycle and increases to 442 Ω after 40 cycles in NIBs. However, this value only increases to 89.7 Ω after 40 cycles in LIBs. The R_{ct} value during cycling in NIBs agree well with the trend in coulombic efficiency and signal of SEI (which is actually a heterogeneous multilayer) formation. The consistently higher R_{ct} in NIBs than that in LIBs can not only be attributed to the

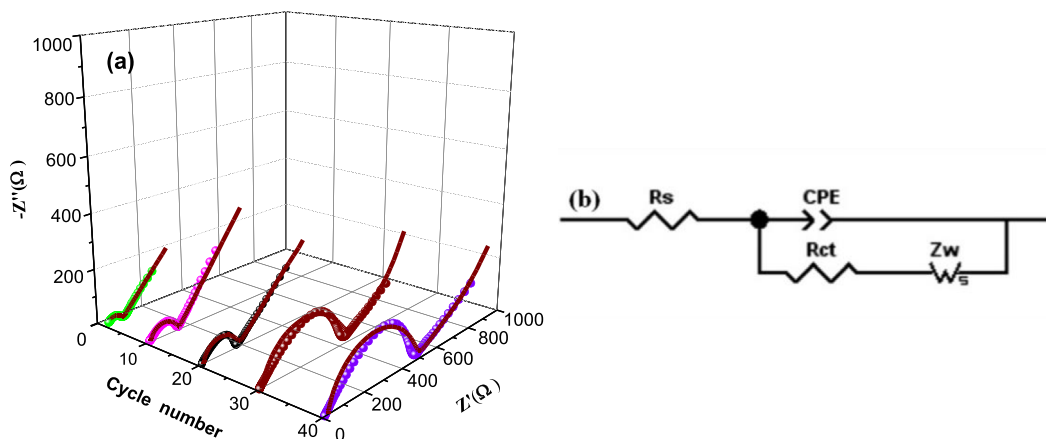


Fig. 10. Three-dimensional Nyquist plots measured for anatase@TiO₂(B) spheres after cycling for different cycles at a current density of 170 mA g⁻¹ in Na half-cells; (b) the equivalent circuit model.

Table 2
 R_s and R_{ct} values of anatase@TiO₂(B) spheres after different cycles in Na half-cells.

Sample	R_s (Ω)					R_{ct} (Ω)				
	1st	10th	20th	30th	40th	1st	10th	20th	30th	40th
Anatase@TiO ₂ (B) bicrystalline	17.2	21.1	21.2	23.0	25.1	75	123	156	390	442

progressive growth of SEI on exposed electrode surfaces but also to the lower sodium ion diffusion, which decrease the conductivity and increase the transfer resistance of the sample. Hence, the EIS results well indicate that the sodium ion with a relative larger ionic radius in NIBs shows a higher polarization than that of lithium ion in LIBs.

4. Conclusions

In summary, anatase@TiO₂(B) spheres have been successfully synthesized via a facile one-pot solvothermal method. SEM and TEM confirm that anatase@TiO₂(B) spheres are consisted of TiO₂(B) nanosheets shell and anatase spheres core which is constituted of TiO₂ nanoparticles. On one hand, the anatase@TiO₂(B) spheres exhibit improved lithium storage properties with enhanced rate capability and super cycling performance. Anatase@TiO₂(B) spheres show high discharge capacity of 160 mAh g⁻¹ and 131.1 mAh g⁻¹ after 100 cycles at rates of 1 and 10 C, respectively. Anatase@TiO₂(B) spheres also deliver stable capacity retention for over 350 cycles at a high rate of 30 C between 1.0 and 3.0 V in LIBs. On the other hand, the excellent electrochemical sodium storage properties of anatase@TiO₂(B) spheres have also been proved. After deep cycling at 850 mA g⁻¹, a capacity of 168.6 mAh g⁻¹ is fully restored upon reducing the rate to 85 mA g⁻¹, and the discharge capacity remains at 131 mAh g⁻¹ at the rate of 170 mA g⁻¹ after 50 cycles between 0.01 V and 2.5 V in NIBs. Anatase@TiO₂(B) spheres show good rate capability and cycle performance as an anode material for the NIBs. All these results suggest that the anatase@TiO₂(B) spheres are promising anode materials not only for Li batteries but also for future Na batteries.

Acknowledgments

This work is supported financially by the National Natural Science Foundation of China (Grant No. 51202209), Doctoral Fund of Ministry of Education of China (Grant No. 20114301120007), and Hunan Provincial Natural Science Foundation of China (Grant No. 14JJ6017).

Appendix A. Supplementary data

Supplementary data related to this article can be found at <http://dx.doi.org/10.1016/j.jpowsour.2014.06.150>.

References

- [1] M. Shirkpour, J. Cabana, M. Doeff, *Energy Environ. Sci.* 6 (2013) 2538.
- [2] F.X. Wu, X.H. Li, Z.X. Wang, H.J. Guo, *Nanoscale* 5 (2013) 6936.
- [3] J.S. Chen, Y.L. Tan, C.M. Li, Y.L. Cheah, D. Luan, S. Madhavi, F.Y.C. Boey, L.A. Archer, X.W. Lou, *J. Am. Chem. Soc.* 132 (2010) 6124.
- [4] V. Palomares, I. Villaluenga, K.B. Hueso, J. Carretero-Gonzalez, T. Rojo, *Energy Environ. Sci.* 5 (2012) 5884.
- [5] Z.S. Wu, W. Ren, L. Wen, L. Gao, J. Zhao, Z. Chen, G. Zhou, F. Li, H.M. Cheng, *ACS Nano* 4 (2010) 3187.
- [6] B. Zhang, Y. Yu, Y.S. Liu, Z.D. Huang, Y.B. He, J.K. Kin, *Nanoscale* 5 (2013) 2100.
- [7] M. Winter, J.O. Besenhard, M.E. Spahr, P. Novák, *Adv. Mater.* 10 (1998) 725.
- [8] H. Marsh, N. Murdie, I.A.S. Edwards, *Carbon* 24 (1986) 267.
- [9] Y. Mikhalev, H.A. Oye, *Carbon* 34 (1996) 37.
- [10] K.M. Abrahm, *Electrochim. Acta* 38 (1993) 1233.
- [11] Z. C. Yan, L. Liu, H.P. Guo, J.L. Tan, H.B. Shu, X.K. Yang, H. Hu, Q. Zhou, Z.F. Huang, X.Y. Wang, *Electrochim. Acta* 123 (2014) 551.
- [12] I.A. Udod, H.B. Orman, V.K. Genchel, *Carbon* 32 (1994) 101.
- [13] S. Flandrois, B. Simon, *Carbon* 37 (1999) 165.
- [14] H.T. Fang, M. Liu, D.W. Wang, T. Sun, D.S. Guan, F. Li, J.G. Zhou, T.K. Sham, H.M. Cheng, *Nanotechnology* 20 (2009) 227501.
- [15] C. Jiang, J. Zhang, *J. Mater. Sci. Technol.* 29 (2012) 97.
- [16] Z. Bi, M.P. Paranthaman, P.A. Menchhofer, R.R. Dehoff, C.A. Bridges, M. Chi, B. Guo, X.G. Sun, S. Dai, *J. Power Sources* 222 (2013) 461.
- [17] H. Xiong, M.D. Slater, M. Balasubramanian, C.S. Johnson, T. Rajh, *J. Phys. Chem. Lett.* 2 (2011) 2560.
- [18] Y. Xu, E.M. Lotfabad, H. Wang, B. Farbod, Z. Xu, A. Kohandehghan, D. Mitlin, *Chem. Commun.* 49 (2013) 8973.
- [19] H.K. Han, T. Song, J.Y. Bae, L.F. Nazar, H.S. Kim, U. Paik, *Energy Environ. Sci.* 4 (2011) 1986.
- [20] Z.H. Chen, I. Belharouak, Y.K. Sun, K. Amine, *Adv. Funct. Mater.* 23 (2013) 959.
- [21] S. Brutti, V. Gentili, H. Menard, B. Scrosati, P.G. Bruce, *Adv. Energy Mater.* 2 (2012) 322.
- [22] S. Liu, H. Jia, L. Han, J. Wang, P. Gao, D. Xu, J. Yang, S. Che, *Adv. Mater.* 24 (2012) 3201.
- [23] J.P. Huang, D.D. Yuan, H.Z. Zhang, Y.L. Cao, G.R. Li, H.X. Yang, X.P. Gao, *RSC Adv.* 3 (2013) 12593.
- [24] H. Zhang, D.Q. Li, G.S. Shao, Z.Y. Yuan, *Sci. China Ser. B* 52 (2009) 1498.
- [25] T.B. Lan, Y.B. Liu, J. Dou, Z.S. Hong, M.D. Wei, J. Mater. Chem. A 2 (2014) 1102.
- [26] L.X. Zeng, C. Zheng, L.C. Xia, Y.X. Wang, M.D. Wei, *J. Mater. Chem. A* 1 (2013) 4293.
- [27] X.M. Yin, C.C. Li, M. Zhang, Q.Y. Hao, S. Liu, L.B. Chen, T.H. Wang, *J. Phys. Chem. C* 114 (2010) 8084.
- [28] J. Jeong, B.G. Choi, S.C. Lee, K.G. Lee, S. Chang, Y. Han, Y.B. Lee, H.U. Lee, S. Kwon, G. Lee, C. Lee, Y.S. Huh, *Adv. Mater.* 25 (2013) 6250.
- [29] J.Y. Xiang, J.P. Tu, L. Zhang, Y. Zhou, X.L. Wang, S.J. Shi, *J. Power Sources* 195 (2010) 313.
- [30] K. Saravanan, K. Ananthanarayanan, P. Balaya, *Energy Environ. Sci.* 3 (2010) 939.
- [31] W. Li, Z. Wu, J. Wang, A.A. Elzatahry, D. Zhao, *Chem. Mater.* 26 (2014) 287.
- [32] J.S. Chen, D. Luan, C.M. Li, S. Qiao, X.W. Lou, *Chem. Commun.* 46 (2013) 8252.
- [33] T. Kasuga, M. Hiramatsu, A. Hoson, T. Sekino, K. Niihara, *Langmuir* 14 (1998) 3160.
- [34] H. Izawa, S. Kikkawa, M. Koizumi, *J. Solid State Chem.* 60 (1985) 264.
- [35] W.A. Daoud, G.K.H. Pang, *J. Phys. Chem. B* 110 (2006) 25746.
- [36] J.F. Zhu, J.L. Zhang, F. Chen, M. Anpo, *Mater. Lett.* 59 (2005) 3378.
- [37] X.W. Lou, L.A. Archer, *Adv. Mater.* 20 (2008) 1853.
- [38] B. Song, S.W. Liu, J.K. Jian, M. Lei, X.J. Wang, H. Li, J.G. Yu, X.L. Chen, *J. Power Sources* 180 (2008) 869.
- [39] S.K. Das, S. Darmakolla, A.J. Bhattacharyya, *J. Mater. Chem.* 20 (2010) 1600.
- [40] H. Lindstrohm, S. So1dergren, A. Solbrand, H. Rensmo, J. Hjelm, A. Hagfeldt, S.E. Lindquist, *J. Phys. Chem. B* 101 (1997) 7717.
- [41] C.H. Sun, X.H. Yang, J.S. Chen, Z. Li, X.W. Lou, C.Z. Li, S.C. Smith, G.Q. Lu, H.G. Yang, *Chem. Commun.* 46 (2010) 6129.
- [42] M. Zukalová, M. Kalbáč, L. Kavan, I. Exnar, M. Graetzel, *Chem. Mater.* 17 (2005) 1248.
- [43] L. Kavan, M. Kalbac, M. Zukalova, I. Exnar, V. Lorenzen, R. Nesper, M. Gratzel, *Chem. Mater.* 16 (2004) 477.
- [44] A.R. Armstrong, C. Arrouvel, V. Gentili, S.C. Parker, M.S. Islam, P.G. Bruce, *Chem. Mater.* 22 (2010) 6426.
- [45] A.S. Dalton, A.A. Belak, A. Van der Ven, *Chem. Mater.* 24 (2012) 1568.
- [46] X.B. Wang, Y. Yan, B. Hao, G. Chen, *ACS Appl. Mater. Interfaces* 5 (2013) 3631.
- [47] H.B. Shu, X.Y. Wang, Q. Wu, B.W. Ju, *Electrochim. Acta* 76 (2012) 120.
- [48] Y. Cui, X.L. Zhao, R.S. Guo, *Mater. Res. Bull.* 45 (2010) 844.
- [49] L. Kavan, J. Rathousky, M. Gratzel, V. Shklover, A. Zukal, *J. Phys. Chem. B* 104 (2000) 12012.